

Compositional Inhomogeneity and Tuneable Thermal Expansion
in Mixed-Metal ZIF-8 Analogues:

SUPPLEMENTARY INFORMATION

Adam F. Sapnik, Harry S. Geddes, Emily M. Reynolds, Hamish H.-M. Yeung*
and Andrew L. Goodwin*

Department of Chemistry, University of Oxford, Inorganic Chemistry Laboratory,
South Parks Road, Oxford OX1 3QR, U.K.

*To whom correspondence should be addressed;

E-mail: hamish.yeung@chem.ox.ac.uk or andrew.goodwin@chem.ox.ac.uk

Contents

1	Synthesis	3
2	Atomic absorption spectroscopy	4
3	Powder diffraction measurements	6
4	Scanning electron microscopy	17
5	Infrared spectroscopy	28
6	Non-negative matrix factorisation analysis	30
7	Reverse Monte Carlo modelling	33
8	References	37

1 Synthesis

All reagents were obtained from commercial suppliers and used as received.

Zn_{1-x}Cd_x(mIm)₂

The Zn_{1-x}Cd_x(mIm)₂ series was synthesised as described previously.^{S1} We combined methanolic solutions of zinc nitrate hexahydrate (Zn(NO₃)₂·6H₂O) (ChemCruz) and cadmium nitrate tetrahydrate (Cd(NO₃)₂·4H₂O) (Sigma Aldrich, 98%) to give a range of reaction mixtures (25 mL) corresponding to nominal Cd stoichiometries $x = 0, 0.1, \dots, 1$. To each mixture we added a methanolic solution (25 mL) of 2-methylimidazole (HmIm) (1.622 g; Sigma Aldrich, 99%) and triethylamine (TEA) (2 g; Alfa Aesar, 99%). In all cases a white suspension formed immediately. Each reaction mixture was transferred to a solvothermal glass vial, sealed, loaded in a conductive aluminium block and heated at 60 °C for 48 h. The process gave smooth suspensions which were subsequently compacted by centrifugation at 13.4×10^3 rpm for 20 min. The supernatant was removed and the solid precipitate washed with methanol and left to dry at room temperature overnight to afford Zn_{1-x}Cd_x(mIm)₂ as a white powder. We verified the phase purity and structure type of each sample using X-ray powder diffraction. For all compositions we found the product to adopt the ZIF-8 structure type, except in the pure-Cd ($x = 1$) case which formed instead as the CdIF-3 polymorph.^{S2}

CdIF-1, Cd(mIm)₂

In order to prepare a sample of CdIF-1, which has the same structure type as ZIF-8, we turned to the alternative solvothermal route developed in Ref. S2. Cadmium acetate dihydrate (Cd(CH₃CO₂)₂·2H₂O) (0.267 g; Sigma Aldrich) and HmIm (0.426 g; Sigma Aldrich) were dissolved in n-butanol (15 mL; Alfa Aesar, 99%) and placed in a 20 mL Teflon-lined autoclave. The reaction mixture was heated at 140 °C for 48 h and allowed to cool to room temperature. The solid precipitate was isolated by filtration, washed with ethanol and dried overnight at room temperature to afford CdIF-1 as very pale yellow crystals.

2 Atomic absorption spectroscopy

Atomic absorption spectroscopy (AAS) was used to determine the Zn/Cd composition of our $\text{Zn}_{1-x}\text{Cd}_x(\text{mIm})_2$ samples. Measurements were carried out on a Varian AA240FS spectrometer, using Perkin Elmer ATOMAX cathode lamps. The lamp current was 10 mA, slit width 0.1 nm and fuel source an acetylene/air mix.

Reference solutions were prepared for Cd and Zn from Acros Organics 1 g/L stock solutions by successive dilution with deionised water. Concentrations were chosen such that they fell in the optimum working range for a given flame emission wavelength:

- (i) For Zn, at 213.9 nm the optimum working range is 0.01–2 μL and the chosen concentrations were: 0.3, 0.6, 0.9, 1.2 and 1.5 mg/L.
- (ii) For Cd, at 228.8 nm the optimum working range is 0.02–3 μL and the chosen concentrations were: 0.5, 1, 1.5, 2, 2.5 and 3 mg/L.

For each sample, a known mass was initially dissolved in concentrated nitric acid and then diluted with deionised water until the concentrations of the metal ions fell within the optimum working range.

Prior to measurement, the lamp and flame positions were optimised. Each measurement was repeated five times to ensure consistency. By comparison with the relevant calibration curve, metal ion concentrations were calculated from the absorption data. The corresponding molar ratios are given in Table S1.

x_{nominal}	x_{AAS}
0.1	0.102(7)
0.2	0.211(4)
0.3	0.298(4)
0.4	0.360(6)
0.5	0.475(5)
0.6	0.532(5)
0.7	0.581(6)
0.8	0.719(5)
0.9	0.872(5)

Table S1: Experimental sample compositions determined by AAS for $\text{Zn}_{1-x}\text{Cd}_x(\text{mlm})_2$.

3 Powder diffraction measurements

Methodology

High-resolution synchrotron X-ray powder diffraction measurements were carried out using the I11 Beamline at the Diamond Light Source. Finely ground samples, mixed with a small amount of silicon as internal standard, were loaded into 0.5 mm borosilicate capillaries and mounted on the diffractometer. Diffraction patterns were collected using the Mythen2 position sensitive detector (PSD) at ambient temperature. The X-ray wavelength was $\lambda = 0.824968 \text{ \AA}$, as calibrated using the silicon NIST 640c standard. Each measurements consisted of two scans of 5 s exposure, offset relative to one another by $\Delta 2\theta = 0.25^\circ$. Our very first measurements showed the series to be sensitive to the X-ray beam damage, and hence our data collection strategy took into account the need to include capillary translations for any successive measurements on individual samples. Doing so ensured that a fresh part of the sample was irradiated for each scan.

Variable-temperature diffraction measurements were carried out using the same instrument for a subset of our $\text{Zn}_{1-x}\text{Cd}_x(\text{mIm})_2$ samples. The sample temperature was controlled using a nitrogen flow Oxford Cryostream. Samples were initially heated to 400 K and left to equilibrate for 10 min to help remove trapped solvent. We then collected diffraction measurements at 30 K intervals over the temperature range 400–100 K. The cooling rate was 6 K s^{-1} .

Pawley refinements were carried out using TOPAS Academic (version 4.1).^{S4} Initially, a modified Thompson-Cox-Hasting pseudo-Voigt (TCHZ) peak shape and a simple axial divergence correction were employed to refine the peak shape for the silicon NIST 640c standard. This peak shape was then constrained in subsequent refinements of sample data. Sample refinements were carried out over the angular range $2\theta = 3\text{--}20^\circ$. Our model included two phases: the silicon standard ($Fd\bar{3}m$, $a \sim 4 \text{ \AA}$) and the ZIF-8-type $\text{Zn}_{1-x}\text{Cd}_x(\text{mIm})_2$ phase ($I\bar{4}3m$, $17 < a < 18 \text{ \AA}$). Crystallite size was calculated using the *LVol_FWHM_CS_G_L* macro in TOPAS Academic, which uses a convolution of a Lorentzian and Gaussian component with an angular dependency of $\cos^{-1}(\theta)$. Crystallite size was used in preference to a strain broadening term as we expect the size contribution to be dominant, as observed in the SEM images. Variable-temperature data were interpreted using sequential Pawley refinements, where the starting structural parameters for each refinement were those obtained for a neighbouring temperature point.

Refinement results

A representative Pawley refinement is illustrated in large format in Fig. S1, and the corresponding fits for the full ensemble of room-temperature powder diffraction data for the $\text{Zn}_{1-x}\text{Cd}_x(\text{mIm})_2$ family is shown in Fig. S2. The corresponding unit cell parameters and estimated crystallite sizes are listed in Table S2.

In Figures S3–S7 we show the experimental variable-temperature powder diffraction data and Pawley fits for the five compositions $x = 0, 0.298(4), 0.475(5), 0.581(6)$, and 1. The corresponding lattice parameters are listed in Table S3.

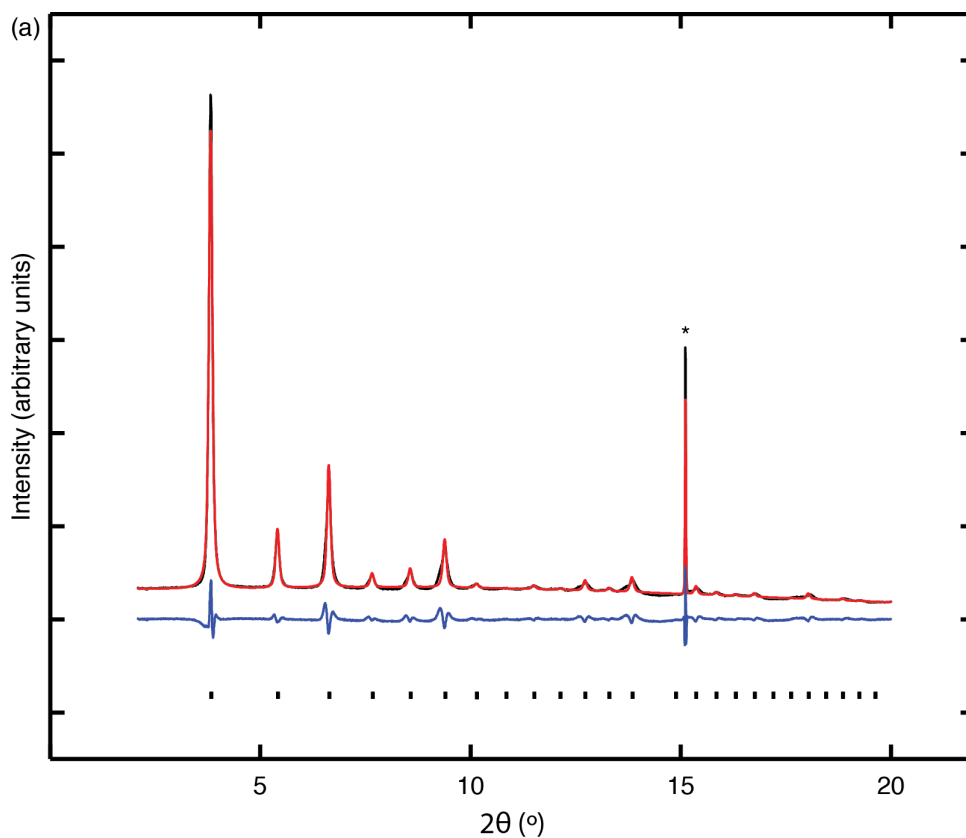


Figure S1: An example Pawley fit of the X-ray diffraction pattern for $x = 0.475(5)$. Synchrotron X-ray diffraction pattern (black lines), Pawley refinement (red lines), difference function (blue lines) and the symmetry-allowed reflections for $\text{Zn}_{1-x}\text{Cd}_x(\text{mIm})_2$ (black tick marks). The peak marked by an asterisk corresponds to silicon.

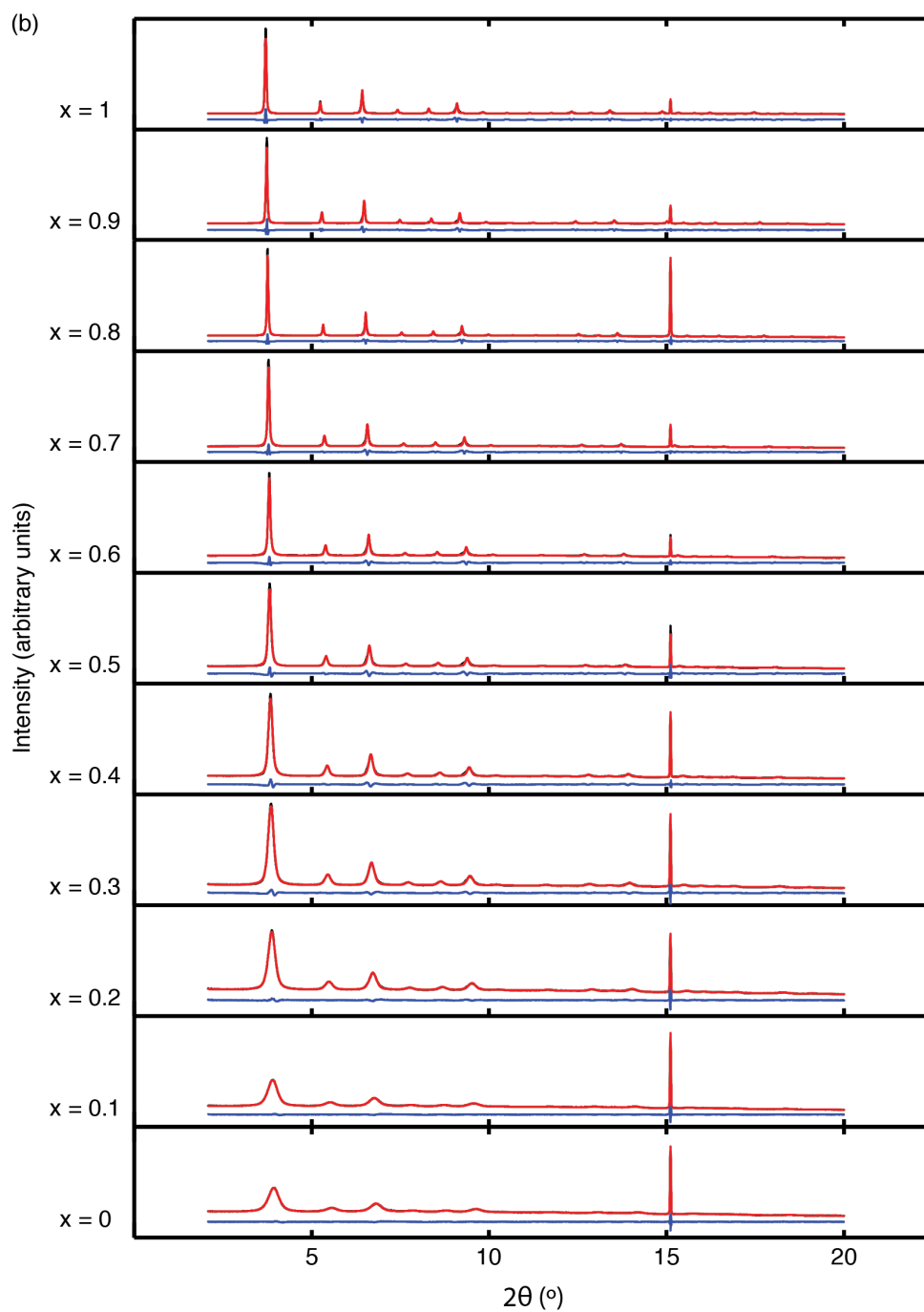


Figure S2: Synchrotron X-ray diffraction patterns (black lines), Pawley refinements (red lines) and difference functions (blue lines) for the $\text{Zn}_{1-x}\text{Cd}_x(\text{mlm})_2$ series at 300 K. Nominal compositions are given on the left-hand side. The sharp peak at $2\theta \sim 15^\circ$ corresponds to silicon.

x	Lattice parameter (Å)	Crystallite size (nm)
0	17.040(3)	9.75(12)
0.102(7)	17.129(2)	10.93(11)
0.211(4)	17.2093(17)	15.14(13)
0.298(4)	17.3167(15)	18.94(15)
0.360(6)	17.3446(14)	26.4(2)
0.475(5)	17.4496(15)	36.0(4)
0.532(5)	17.4954(10)	49.1(6)
0.581(6)	17.5960(9)	62.8(9)
0.719(5)	17.7337(6)	97.1(18)
0.872(5)	17.8462(6)	84.9(12)
1	18.0173(7)	79.5(12)

Table S2: Structural details for the $\text{Zn}_{1-x}\text{Cd}_x(\text{mlm})_2$ series obtained by Pawley refinement against PXRD data collected at 300 K.

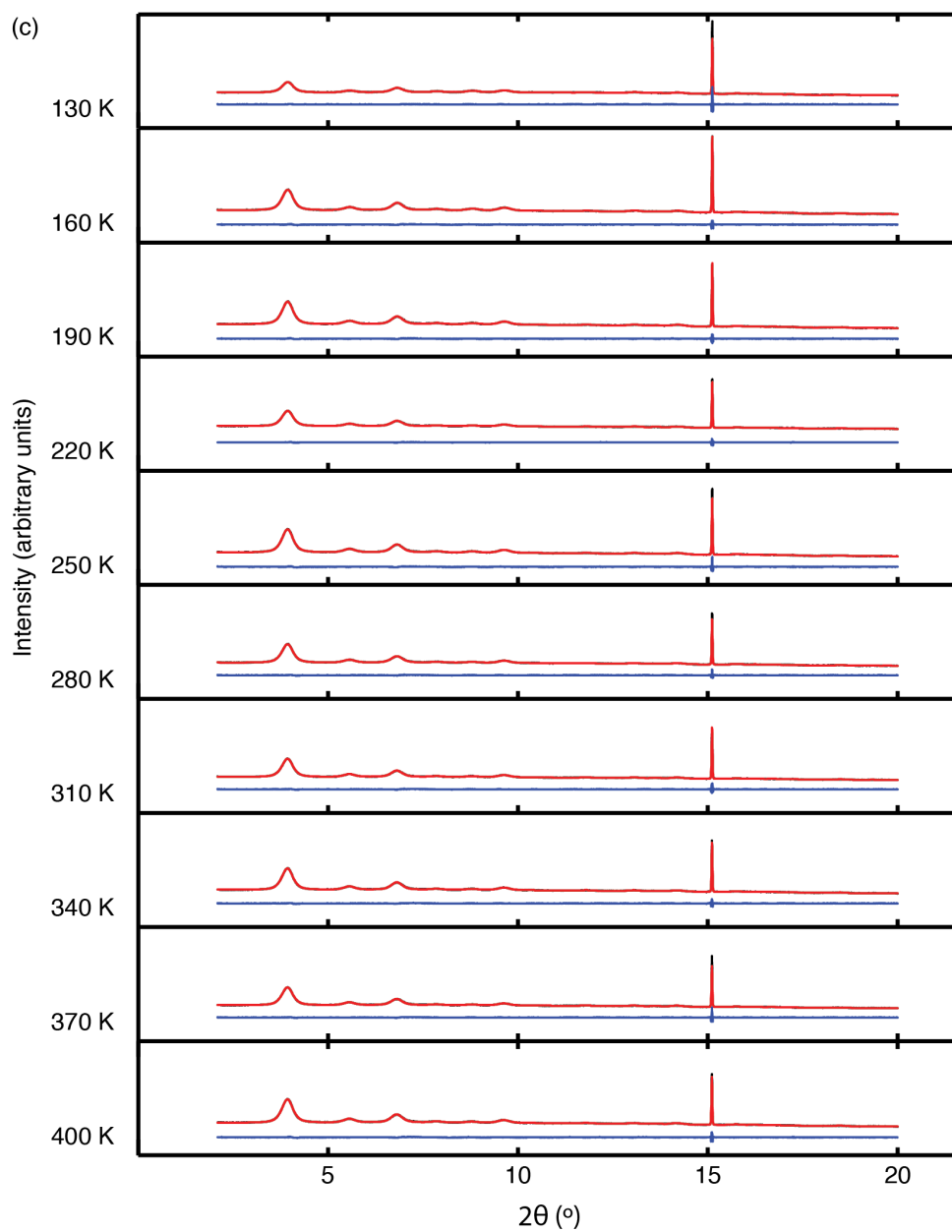


Figure S3: Variable-temperature synchrotron X-ray diffraction patterns (black lines), Pawley refinements (red lines) and difference functions (blue lines) for $x = 0$. The sharp peak at $2\theta \sim 15^\circ$ corresponds to silicon.

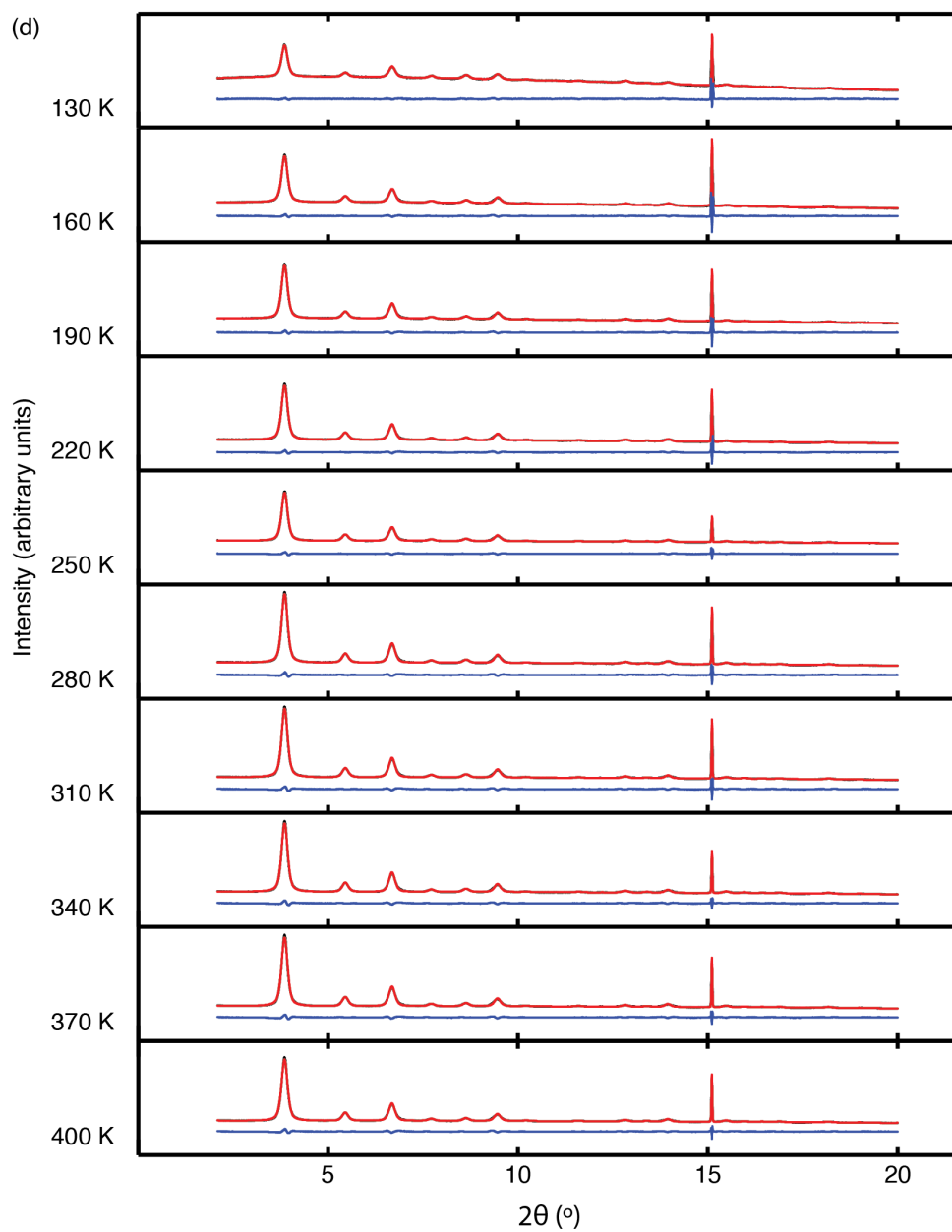


Figure S4: Variable-temperature synchrotron X-ray diffraction patterns (black lines), Pawley refinements (red lines) and difference functions (blue lines) for $x = 0.298(4)$. The sharp peak at $2\theta \sim 15^\circ$ corresponds to silicon.

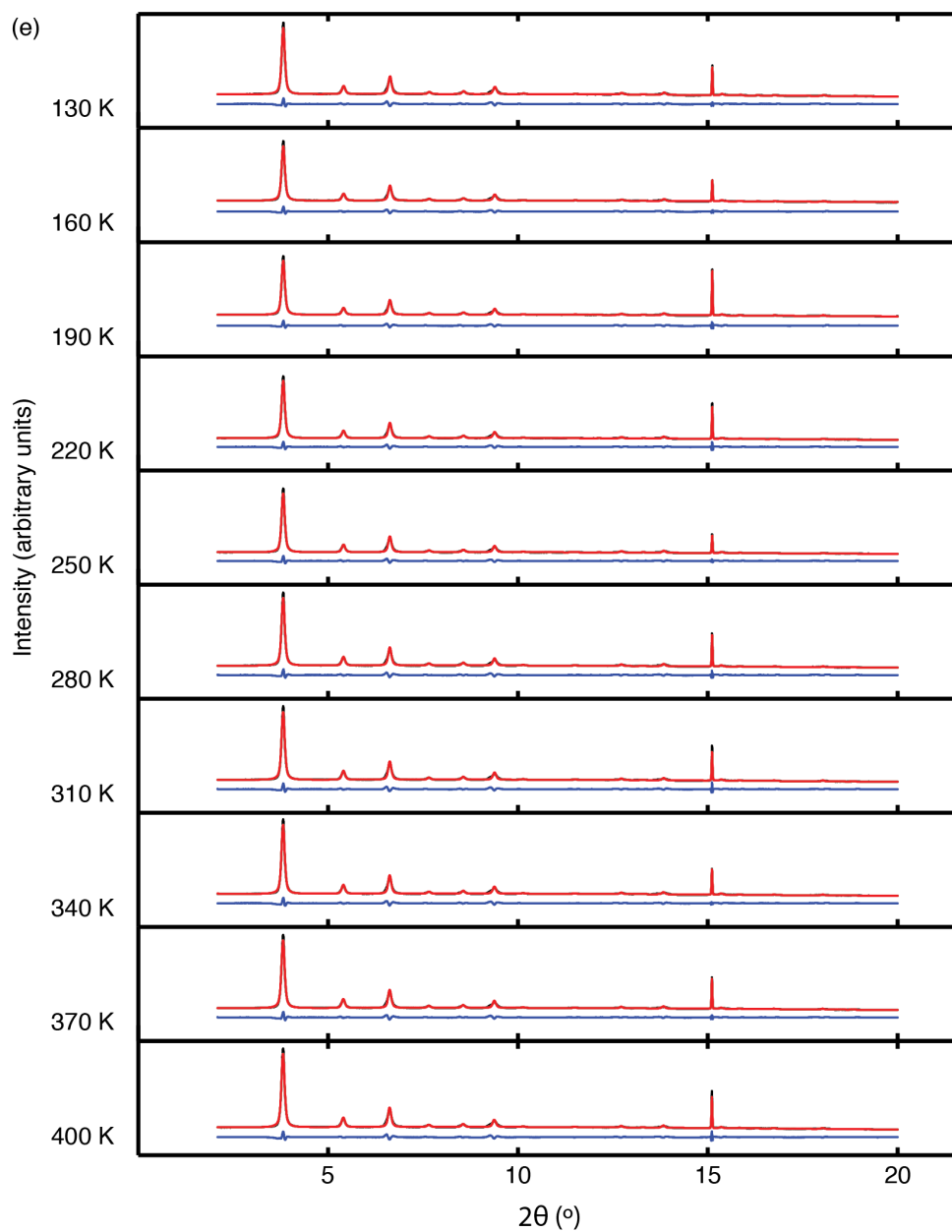


Figure S5: Variable-temperature synchrotron X-ray diffraction patterns (black lines), Pawley refinements (red lines) and difference functions (blue lines) for $x = 0.475(5)$. The sharp peak at $2\theta \sim 15^\circ$ corresponds to silicon.

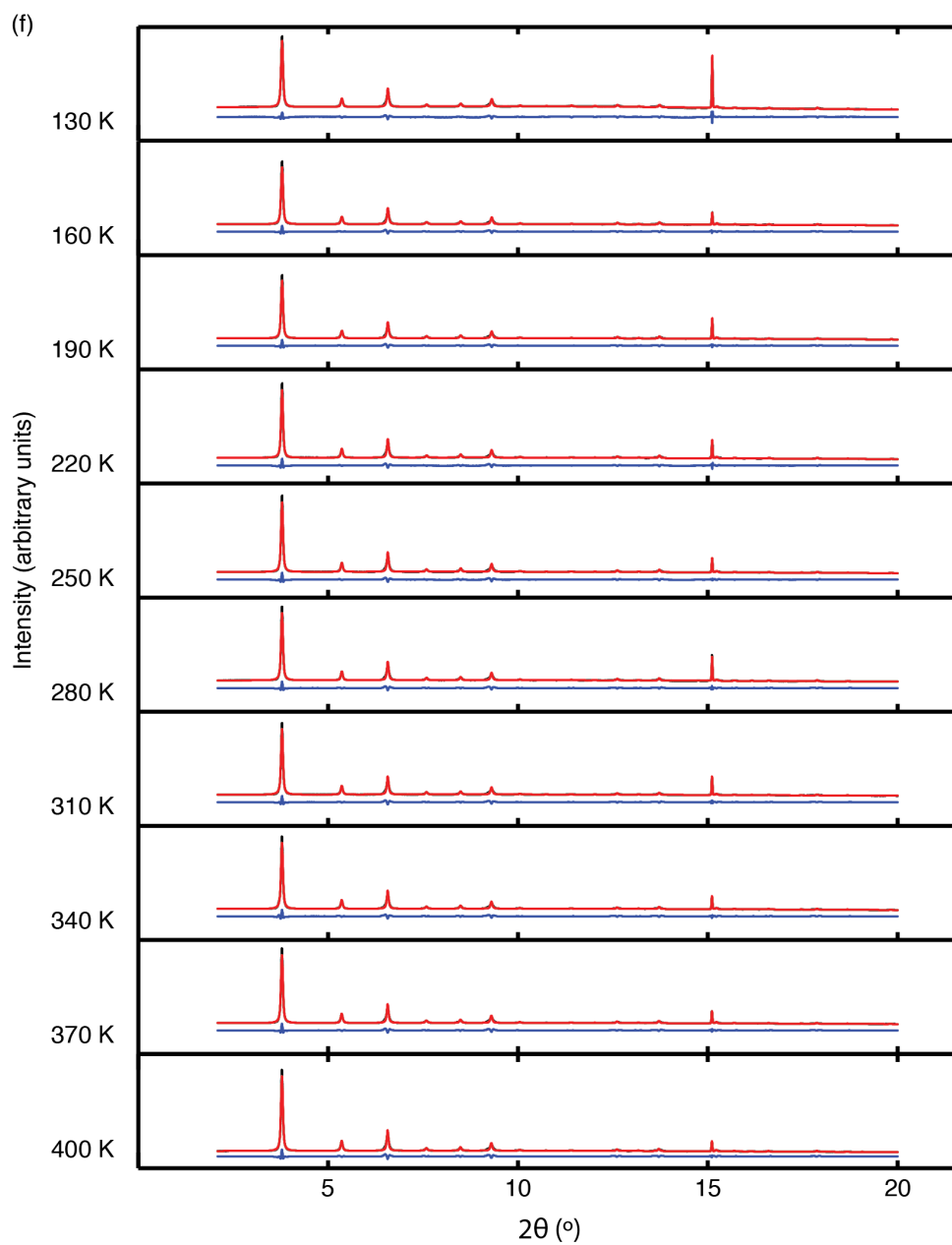


Figure S6: Variable-temperature synchrotron X-ray diffraction patterns (black lines), Pawley refinements (red lines) and difference functions (blue lines) for $x = 0.581(6)$. The sharp peak at $2\theta \sim 15^\circ$ corresponds to silicon.

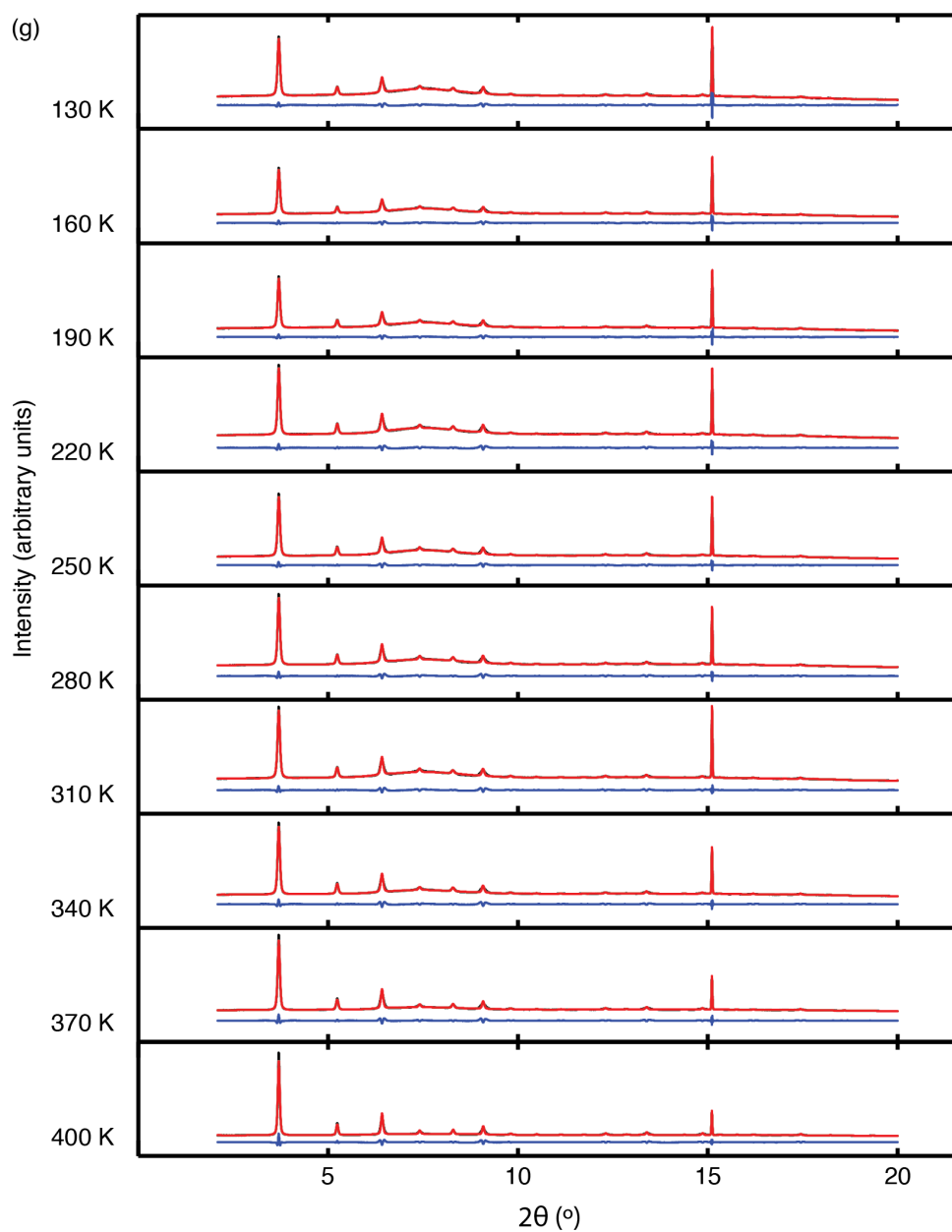


Figure S7: Variable-temperature synchrotron X-ray diffraction patterns (black lines), Pawley refinements (red lines) and difference functions (blue lines) for $x = 1$. The sharp peak at $2\theta \sim 15^\circ$ corresponds to silicon.

Temperature (K)	$x = 0$	$x = 0.298(4)$	$x = 0.475(5)$	$x = 0.581(6)$	$x = 1$
400	17.041(3)	17.3150(14)	17.4535(14)	17.6053(8)	18.0338(9)
370	17.035(3)	17.3147(14)	17.4523(14)	17.6038(8)	18.0427(11)
340	17.023(3)	17.3144(14)	17.4484(14)	17.5988(8)	18.0492(12)
310	17.021(3)	17.3101(16)	17.4448(14)	17.5957(8)	18.0517(12)
280	17.009(3)	17.3042(16)	17.4423(14)	17.5930(8)	18.0470(12)
250	17.006(3)	17.3033(16)	17.4373(13)	17.5899(8)	18.0462(12)
220	17.002(3)	17.297(2)	17.4341(14)	17.5875(8)	18.0450(12)
190	16.995(2)	17.284(3)	17.4316(14)	17.5857(8)	18.0416(13)
160	16.990(2)	17.277(3)	17.4284(13)	17.5831(8)	18.0390(13)
130	16.994(4)	17.286(3)	17.4235(13)	17.582(1)	18.0384(16)
100	–	–	17.426(4)	–	18.0320(13)

Table S3: Unit cell parameters for the $\text{Zn}_{1-x}\text{Cd}_x(\text{mlm})_2$ series as obtained by Pawley refinement against variable-temperature PXRD data.

Thermal expansion calculations

Coefficients of thermal expansion were determined from our variable-temperature unit cell data using the program PASCAL.^{S3} On inspection it was clear that the data for $T > 310$ K included effects from continued desolvation, and so we used only the data $100 \leq T \leq 310$ K for our analysis. The corresponding coefficients of thermal expansion are given in Table S4.

x	α (MK ⁻¹)
0	11.9(17)
0.298(4)	11.2(19)
0.475(5)	6.3(3)
0.581(6)	4.4(3)
1	4.5(4)

Table S4: Coefficients of thermal expansion, α , for the $\text{Zn}_{1-x}\text{Cd}_x(\text{mlm})_2$ series as determined using variable-temperature X-ray powder diffraction measurements.

4 Scanning electron microscopy

Samples were finely ground and dispersed in methanol before being deposited onto 12.5 mm aluminium pin stubs, dried and sputter coated with platinum to allow a conduction path to the ground and prevent the sample from charging. Images were captured using a Carl Zeiss Merlin field emission gun scanning electron microscope with current 500 pA at 5.00 kV under a 10^{-6} mbar vacuum with the SmartSEM software. Representative SEM images for our various samples are shown in Figures S8–S18.

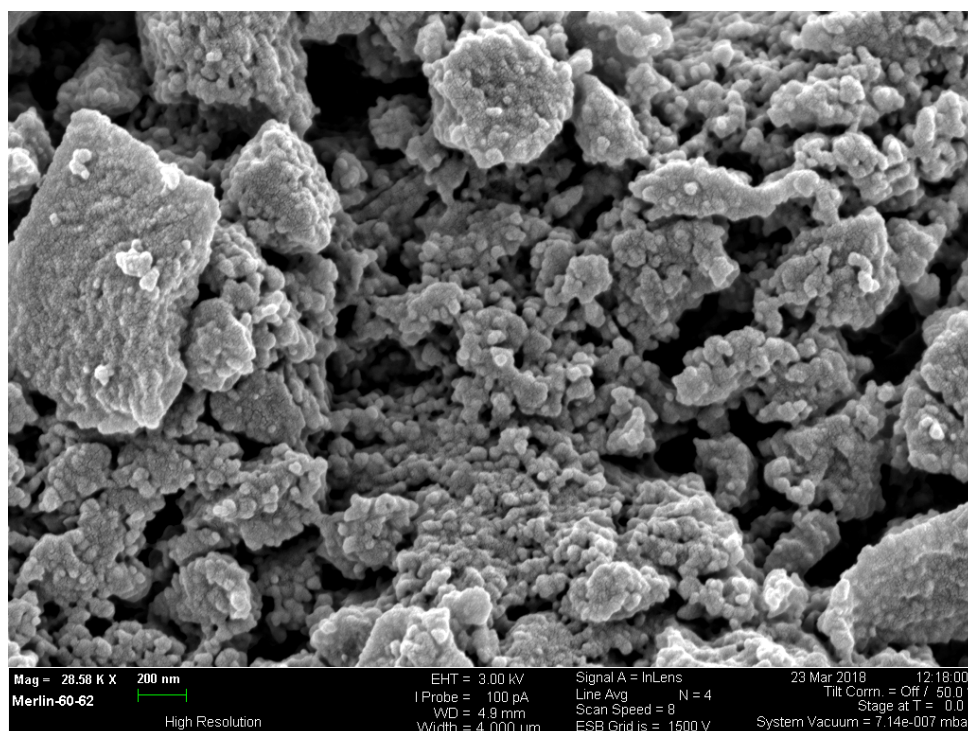


Figure S8: SEM image of $\text{Zn}_{1-x}\text{Cd}_x(\text{mlm})_2$ for $x = 0$.

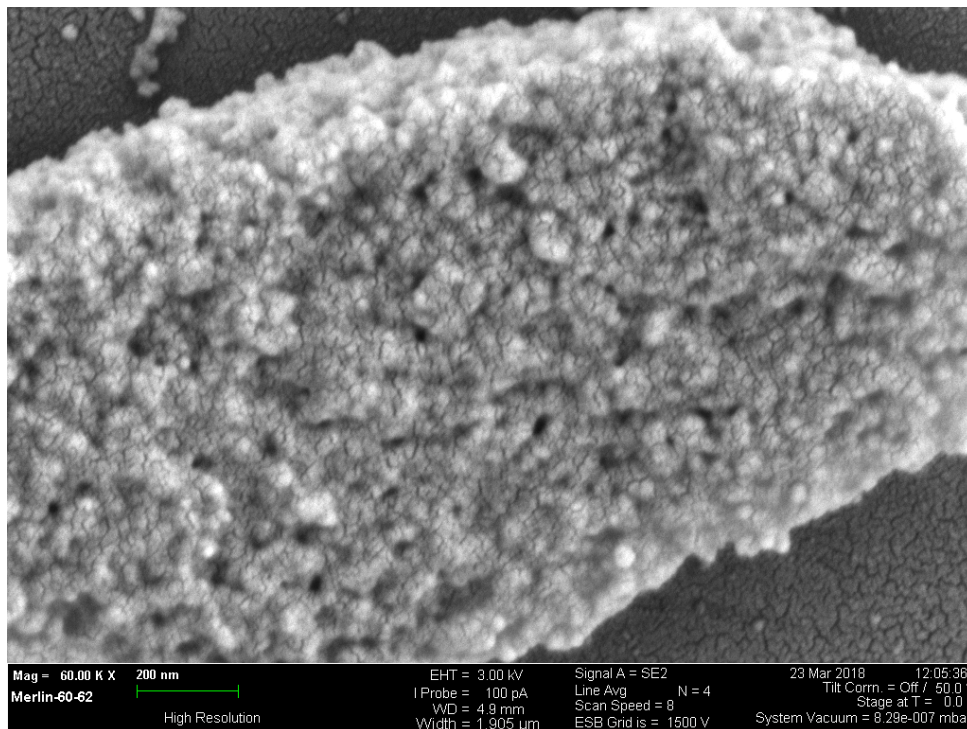


Figure S9: SEM image of $\text{Zn}_{1-x}\text{Cd}_x(\text{mlm})_2$ for $x = 0.102(7)$.

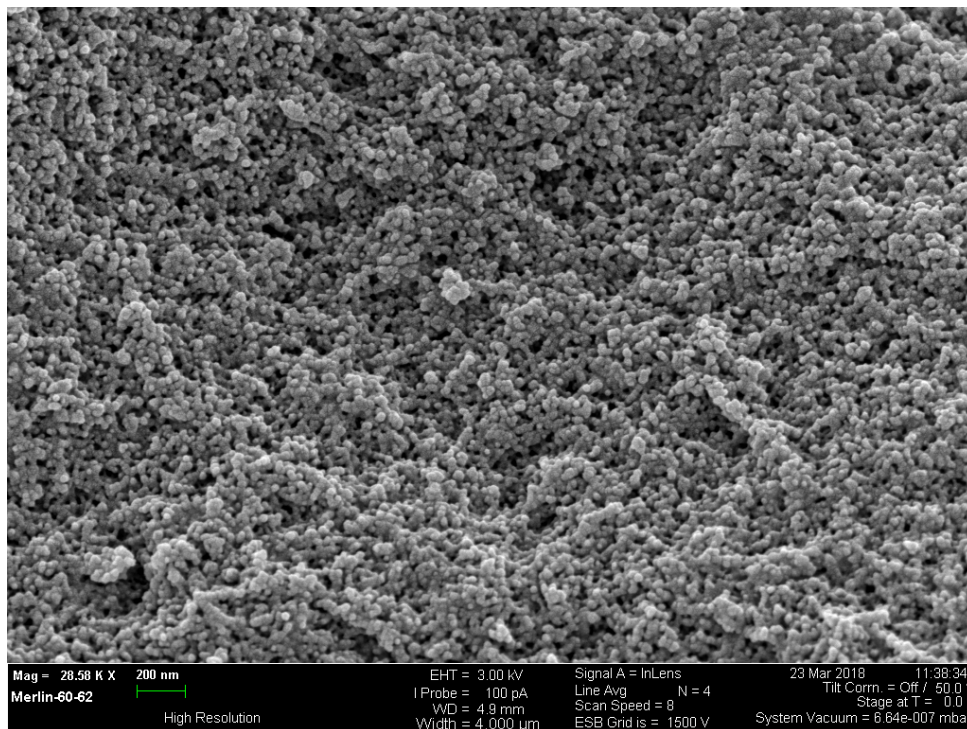


Figure S10: SEM image of $\text{Zn}_{1-x}\text{Cd}_x(\text{mlm})_2$ for $x = 0.211(4)$.

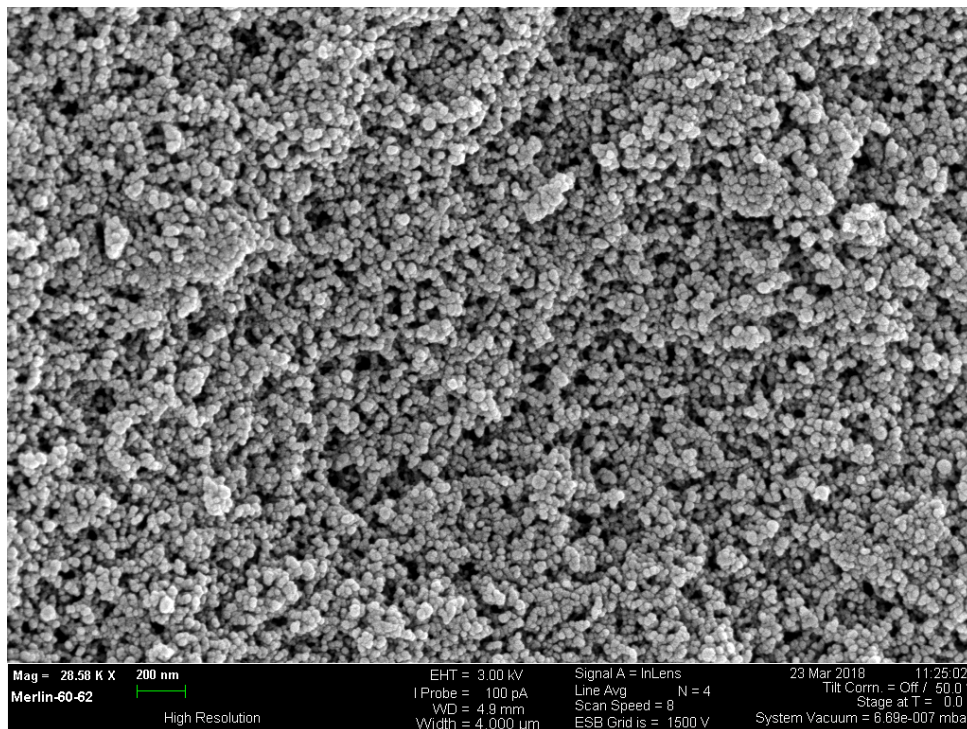


Figure S11: SEM image of $\text{Zn}_{1-x}\text{Cd}_x(\text{mlm})_2$ for $x = 0.298(4)$.

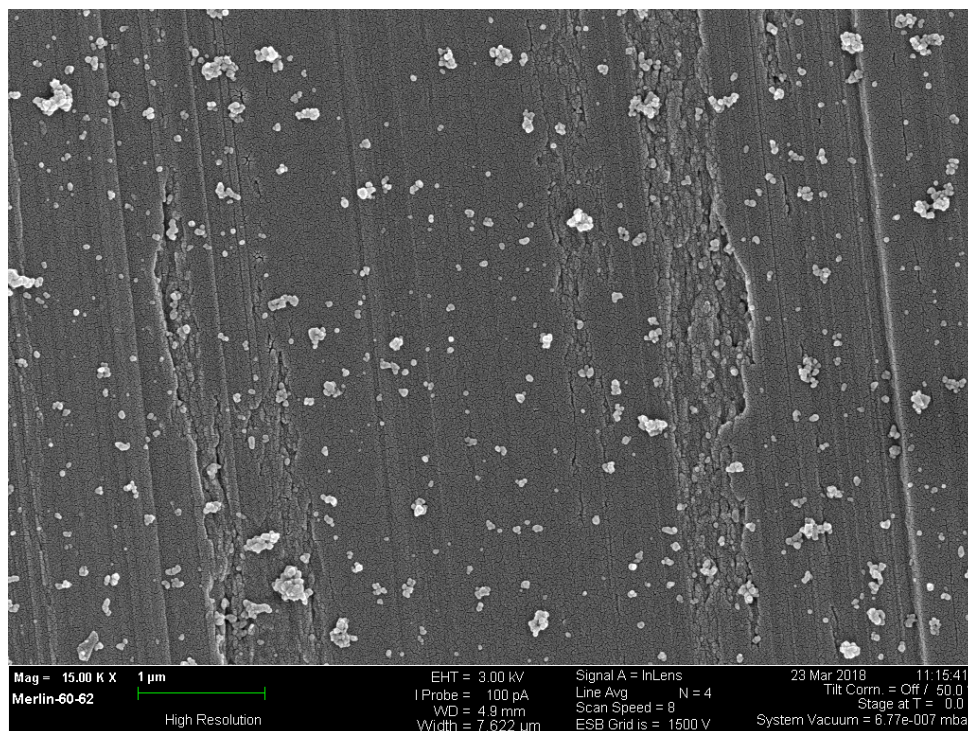


Figure S12: SEM image of $\text{Zn}_{1-x}\text{Cd}_x(\text{mlm})_2$ for $x = 0.360(6)$.

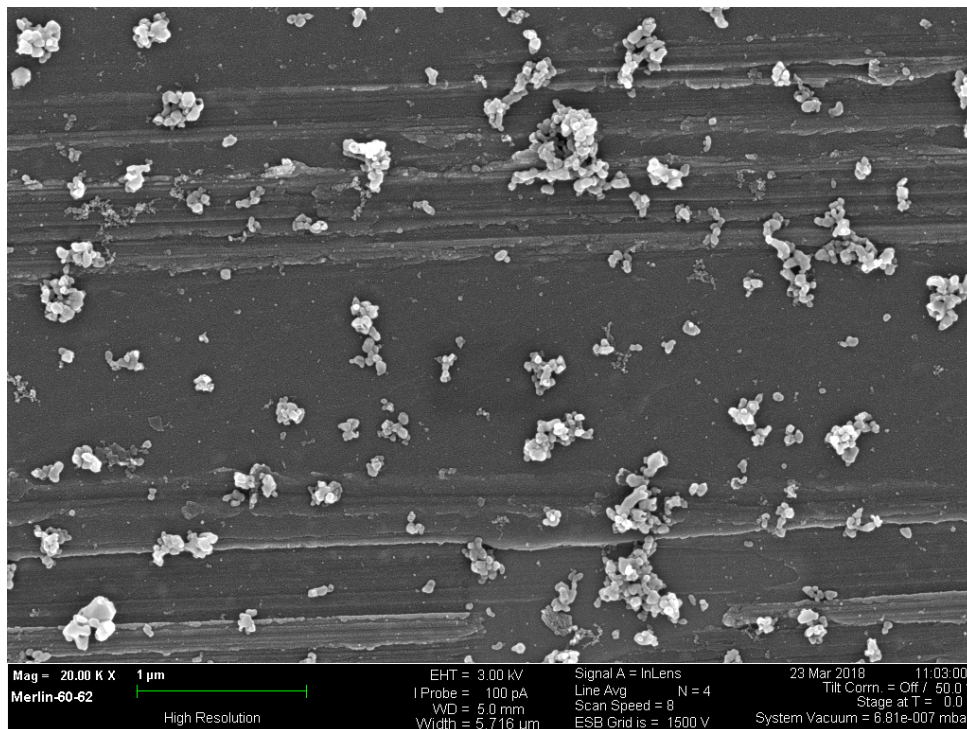


Figure S13: SEM image of $\text{Zn}_{1-x}\text{Cd}_x(\text{mlm})_2$ for $x = 0.475(5)$.

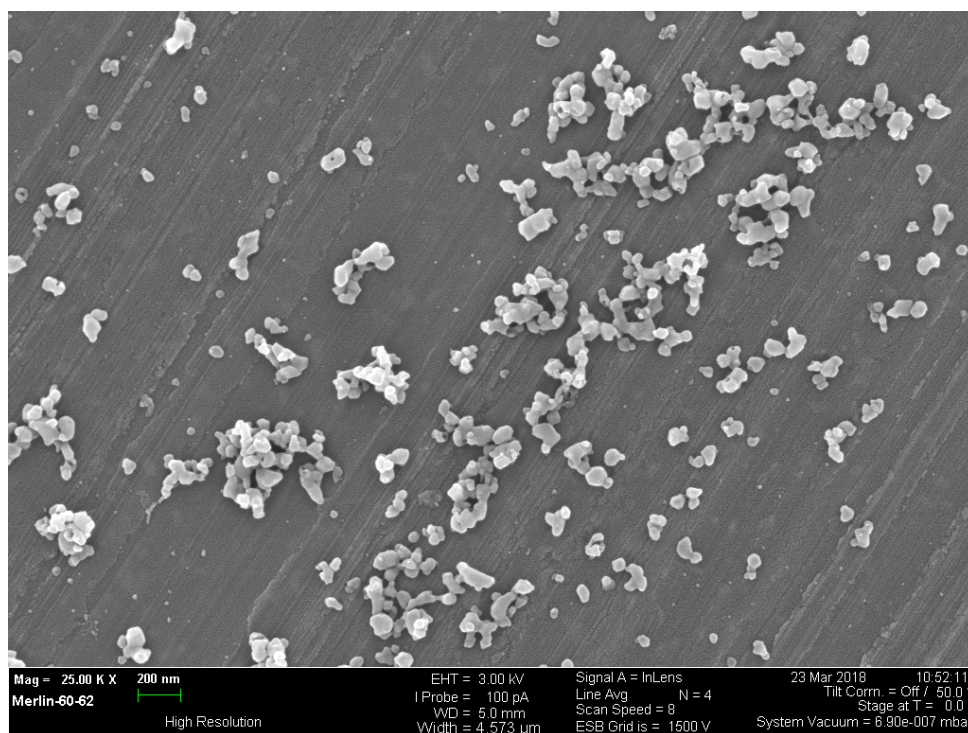


Figure S14: SEM image of $\text{Zn}_{1-x}\text{Cd}_x(\text{mlm})_2$ for $x = 0.532(5)$.

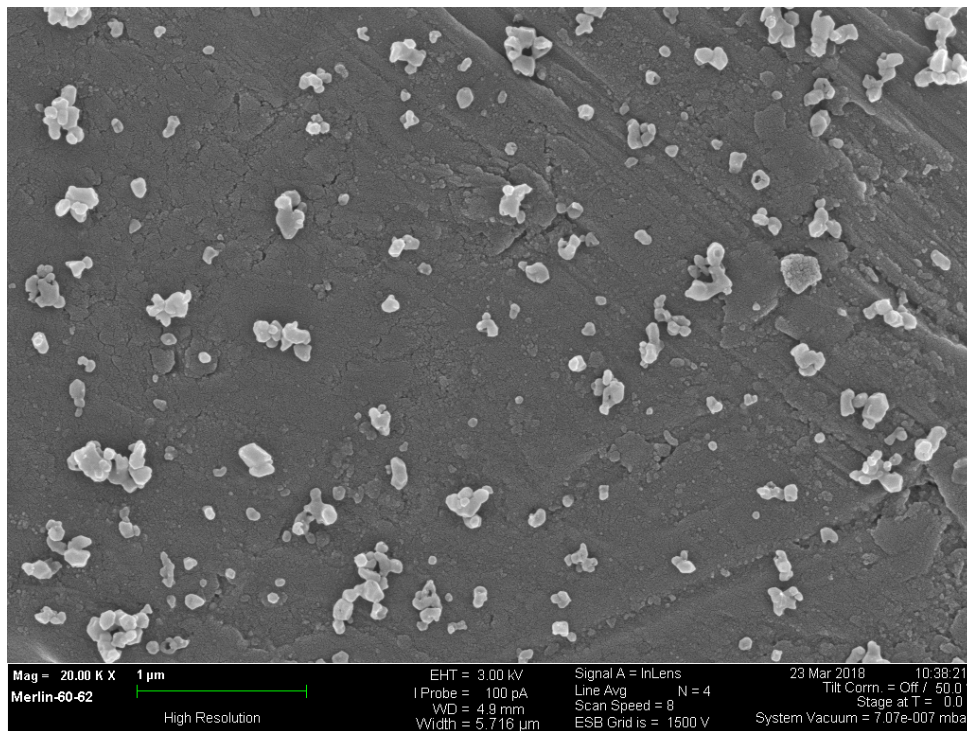


Figure S15: SEM image of $\text{Zn}_{1-x}\text{Cd}_x(\text{mlm})_2$ for $x = 0.581(6)$.

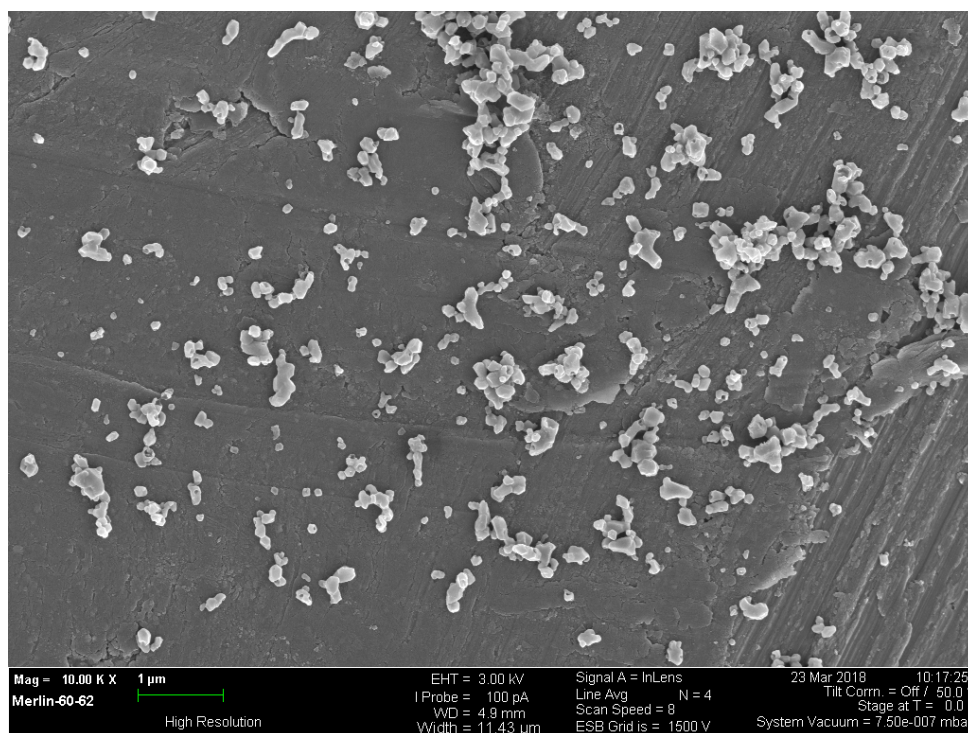


Figure S16: SEM image of $\text{Zn}_{1-x}\text{Cd}_x(\text{mlm})_2$ for $x = 0.719(5)$.

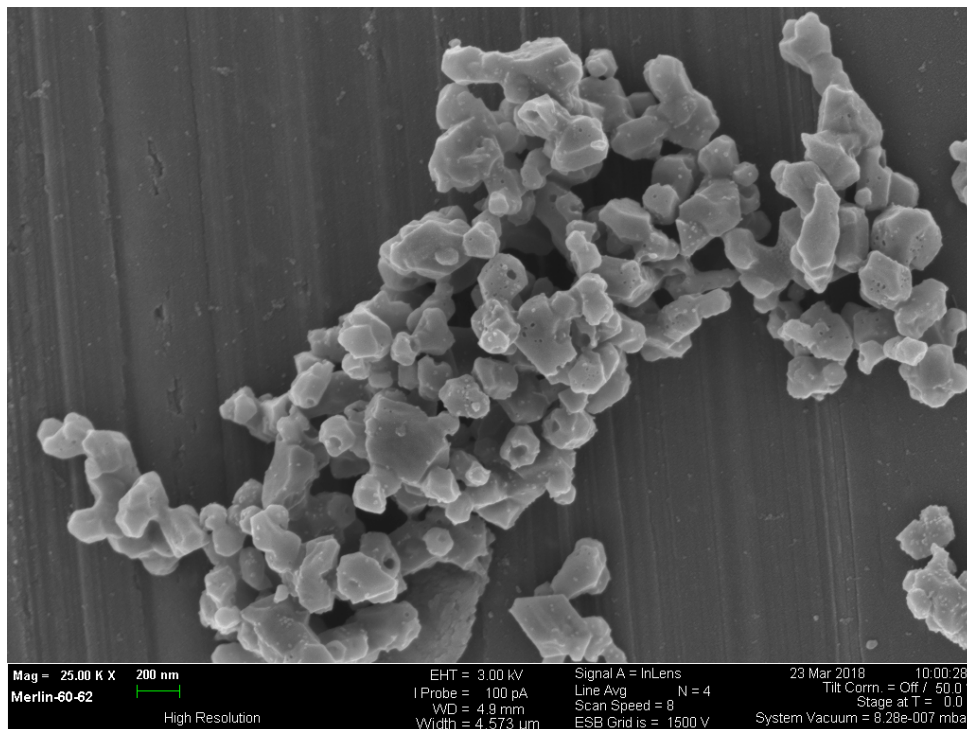


Figure S17: SEM image of $\text{Zn}_{1-x}\text{Cd}_x(\text{mlm})_2$ for $x = 0.872(5)$.

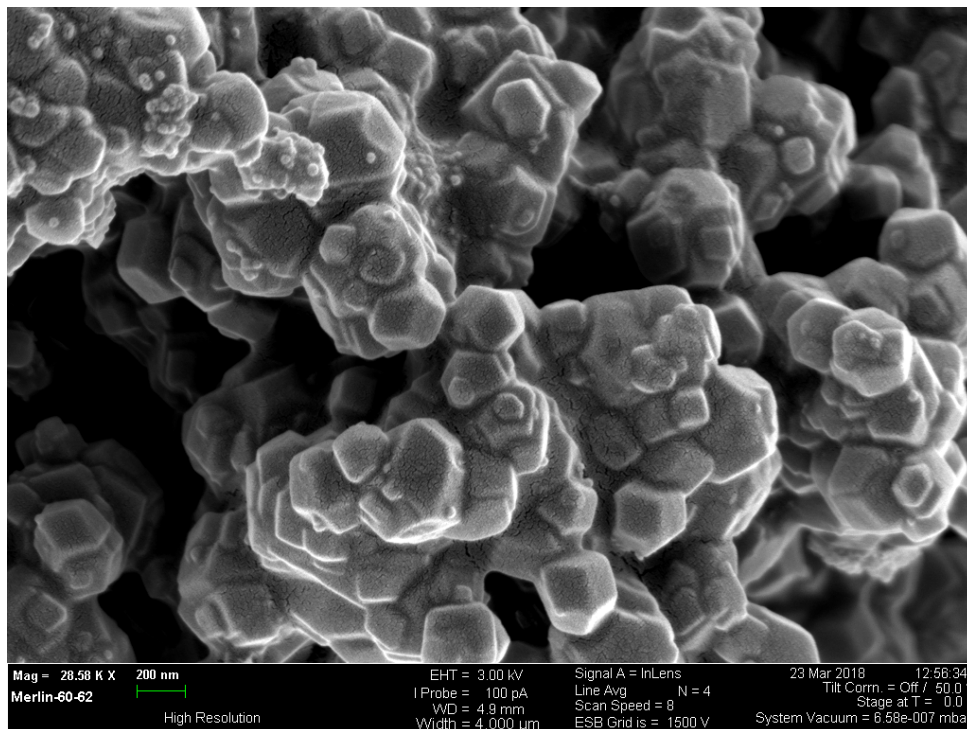


Figure S18: SEM image of $\text{Zn}_{1-x}\text{Cd}_x(\text{mlm})_2$ for $x = 1$.

5 Infrared spectroscopy

Infrared spectroscopy measurements were performed using a Bruker Tensor 27 FT-IR spectrometer, fitted with a diamond attenuated total reflection (ATR) module. The instrument was cleaned with isopropyl alcohol before measuring an initial background scan. A small amount of powder was placed onto the diamond module and secured by the high pressure tower. The instrument was operated with OPUS data collection software and data was collected at room temperature in the range $4700\text{-}650\text{ cm}^{-1}$ with a resolution of 0.5 cm^{-1} . The full IR spectra for our endmember samples ($x = 0, 1$) are shown in Fig. S19. In this figure, we highlight the in-plane bending region used for subsequent analysis as described in the main text.

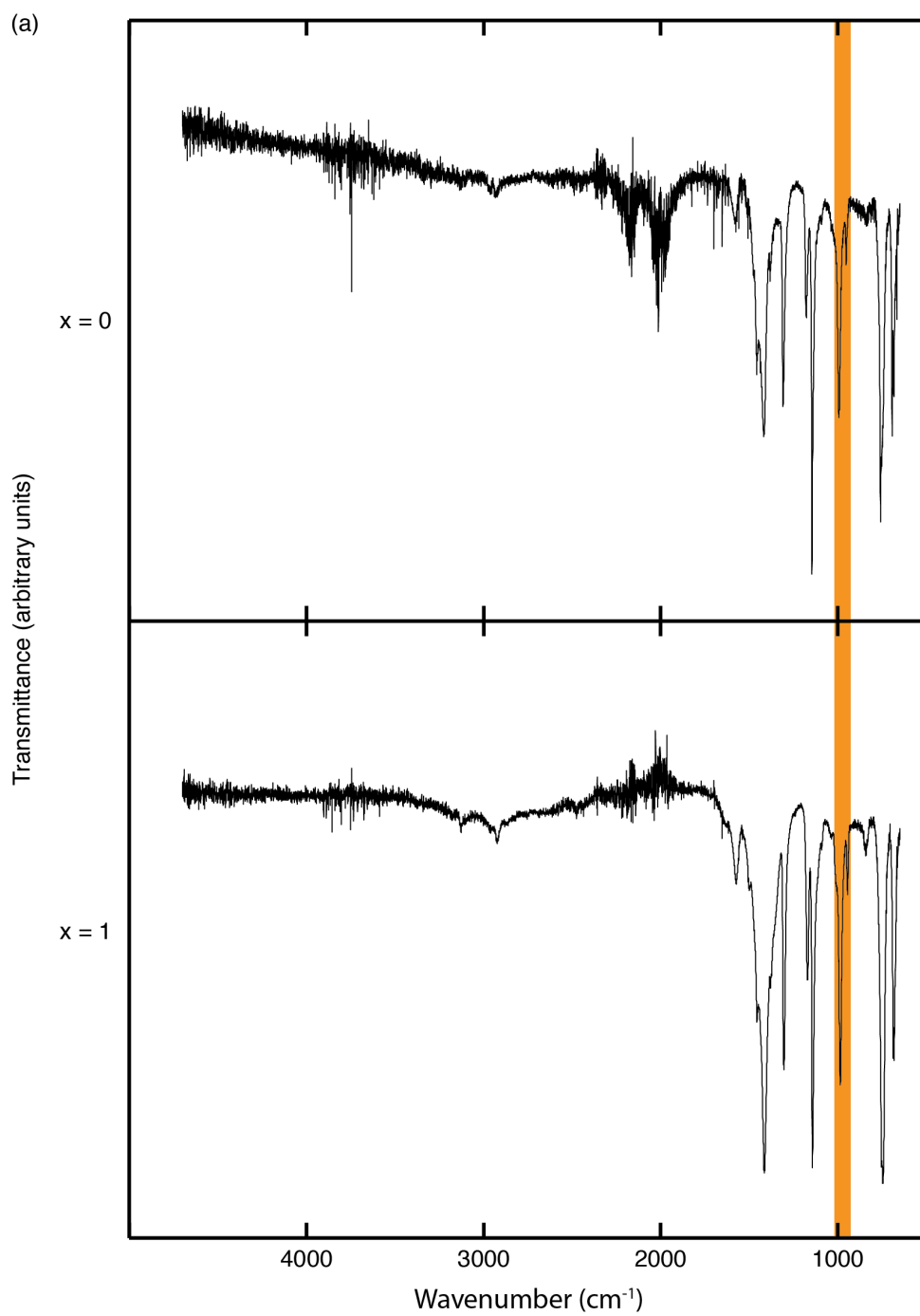


Figure S19: IR spectra for $x = 0$ (top) and $x = 1$ (bottom). Shaded region highlights the in-plane bending mode of the imidazolate ion.

6 Non-negative matrix factorisation analysis

In order to determine the experimental distribution of Cd and Zn as a function of composition, we carried out non-negative matrix factorisation (NMF) analysis of infrared (IR) data using a custom implementation of the NMF algorithm.^{S5-7}

The measured IR spectra were transformed for use in NMF as follows. First, a linear baseline corresponding to the endpoints of the data was defined and subtracted for each IR absorption spectrum in the 930–1015 cm^{-1} region. The resulting absorbances were then inverted (to ensure the non-negative constraint of NMF is satisfied) and normalised. The normalised data themselves are shown in Fig. S20. We have focussed on the 930–1015 cm^{-1} region because it contains the in-plane bending mode of the imidazolate ion, which showed a systematic variation with composition and did not contain overlap with other absorption features. We rationalised that imidazolate in-plane bending frequencies should be sensitive to the nature of the two cations to which an imidazolate anion is bound, and hence allow characterisation of the distribution of Zn–mIm–Zn, Zn–mIm–Cd and Cd–mIm–Cd linkages in our samples.

Using the implementation of NMF developed in Ref. S7, we deconvoluted each IR absorption profile into three components: two were constrained to equal the endmember spectra (*i.e.* corresponding to in-plane bending motion of Zn–mIm–Zn and Cd–mIm–Cd linkages) and the third was allowed to refine freely in order to best fit the ensemble of IR data. This refineable component was initialised with random values in the range 0–1. The approach we have taken ensures the features of each endmember is preserved and we can also account for mixed-metal linkages (Zn–mIm–Cd) *via* the third component. The third component is then varied using a Metropolis Monte Carlo (MC) algorithm.^{S8} Finally, the relative weighting that each of the three components contributes to each IR profile is initialised to the expected values for a simple two-phase system. The weightings are then also altered using a MC algorithm, while satisfying the constraints that the sum of the three weighting terms for each IR profile sums to 1 and are mass balanced according to the experimentally determined (AAS) compositions. Initialisation of the relative contributions increases the speed of convergence to a solution and lowers the risk of converging on local minima. Repeated calculations yielded identical results.

As an additional check of the validity of this approach, we show in Fig. S21 the quality of fits obtained if our IR data are interpreted in terms of linear combinations of the end-member IR traces, weighted according to the corresponding composition. In this way we assess the extent to which our data are explainable purely in terms of in-plane bending motion of homometallic Zn–mIm–Zn and Cd–mIm–Cd linkages. We find a systematic error in the fit for intermediate compositions that reveals a missing

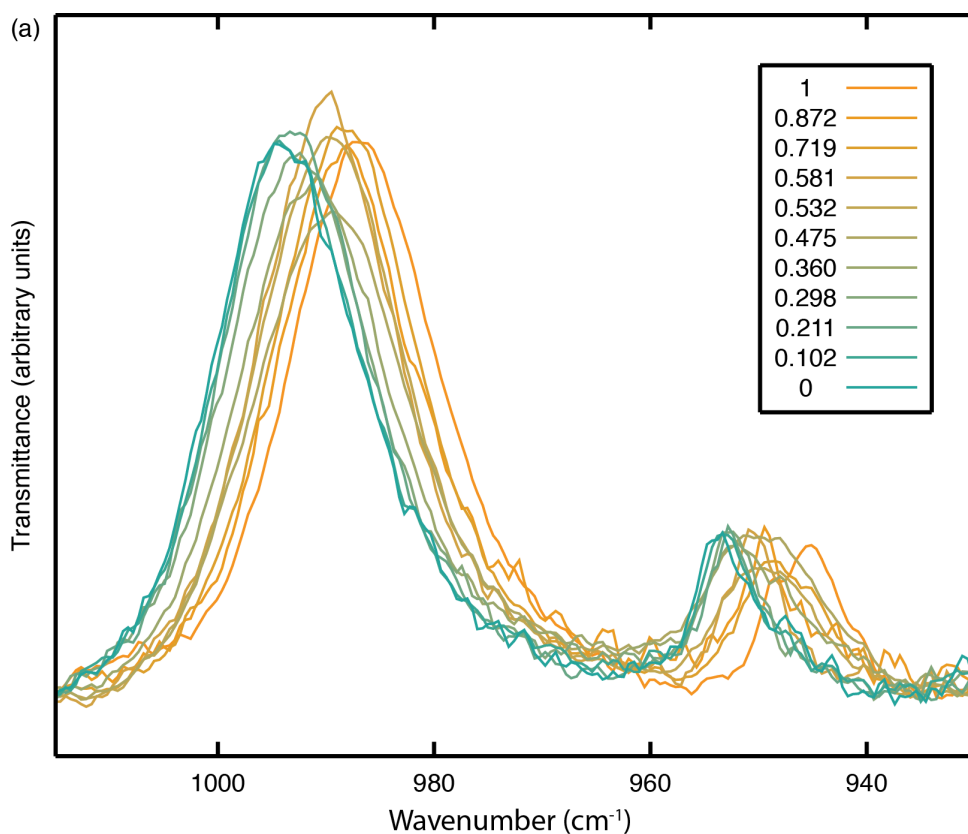


Figure S20: Normalised IR data for the in-plane bending mode region of the imidazolate ion.

third component with maxima at frequencies for which the NMF-refined component also has maxima.

The average R -factor, defined as

$$R = \frac{\sum |I_{\text{obs}} - I_{\text{calc}}|}{\sum I_{\text{obs}}}, \quad (1)$$

reduced from 15% to 13.5% on inclusion of the third (Zn–mIm–Cd) NMF component. Consequently we can be confident of the presence of heterometallic Zn–mIm–Cd linkages in our intermediate-composition samples, and in the ability of NMF to quantify this component.

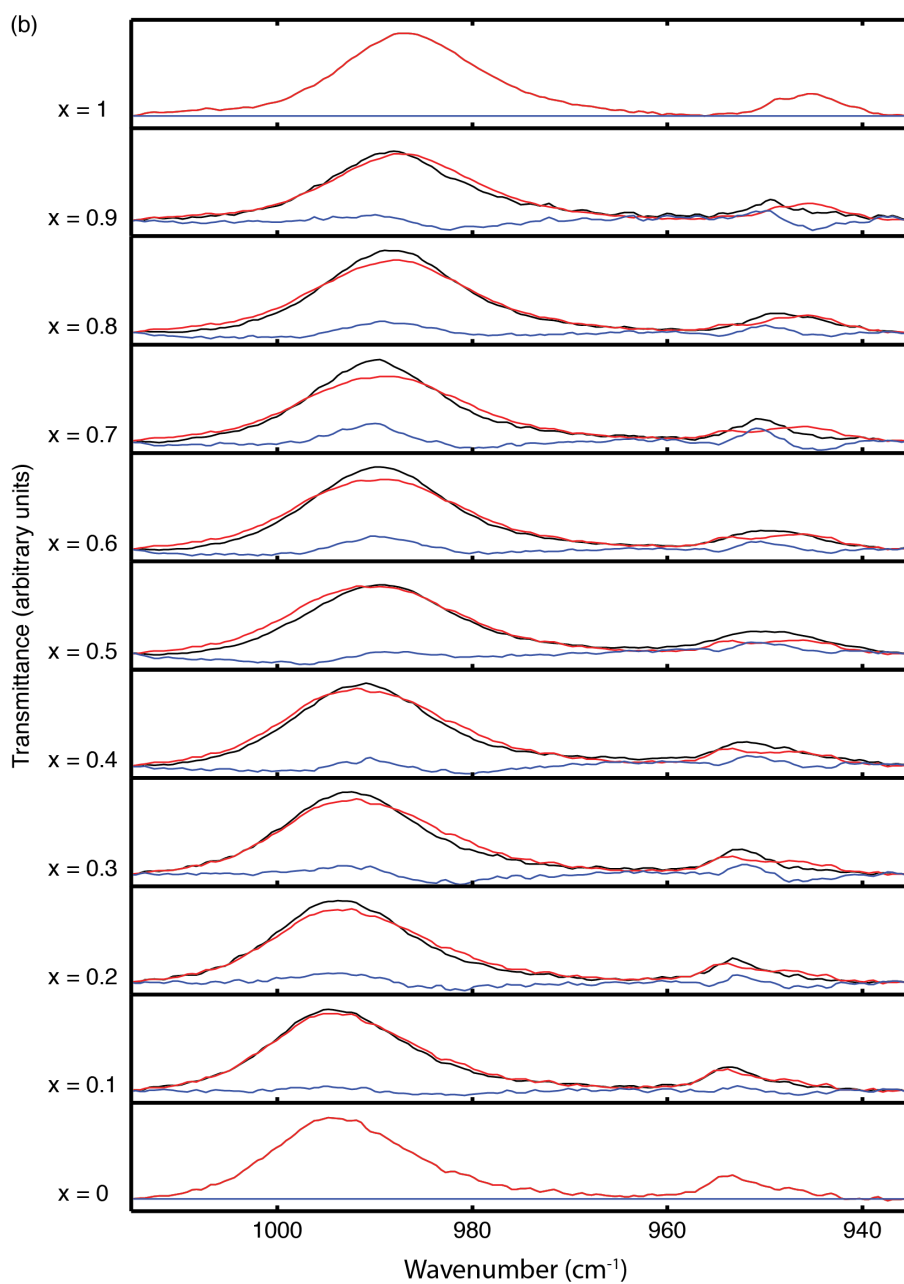


Figure S21: Normalised IR data for the in-plane bending mode region of the imidazolate ion (black), mass balanced linear combinations of the two end members (red), and difference functions between the experimental and reconstructed data (blue). Nominal compositions are given on the left-hand side. The difference function is largest for intermediate compositions, suggesting the IR data is sensitive to the heterometallic Cd–mIm–Zn linkage.

7 Reverse Monte Carlo modelling

In order to understand the microscopic implications of the linker distributions determined in our IR/NMF analysis, we used a Reverse Monte Carlo (RMC) approach.^{S9} The basic idea was to generate an atomistic supercell of the ZIF-8 structure type containing a fixed number of Zn and Cd sites according to the composition of interest. The fraction of Zn–Zn, Zn–Cd, and Cd–Cd neighbours can be calculated straightforwardly from such a model. We then used the Metropolis Monte Carlo algorithm^{S8} to swap Zn and Cd atoms until the configuration reproduced the experimental linker distributions. Hence the resulting RMC configurations are representative states consistent with experimental IR data, and are physically meaningful irrespective of the precise extent to which the experimental systems are at equilibrium. Having assigned Zn/Cd sites, we included a structural ‘relaxation’ step in which Zn and Cd positions were allowed to vary by small amounts such that connected Zn...Zn, Zn...Cd, and Cd...Cd distances were as close as possible to the values expected on the basis of the endmember structures and Vegard’s law. Representative relaxed configurations for three compositions $x = 0.2, 0.5, 0.8$ are shown in Figs. S22–S24.

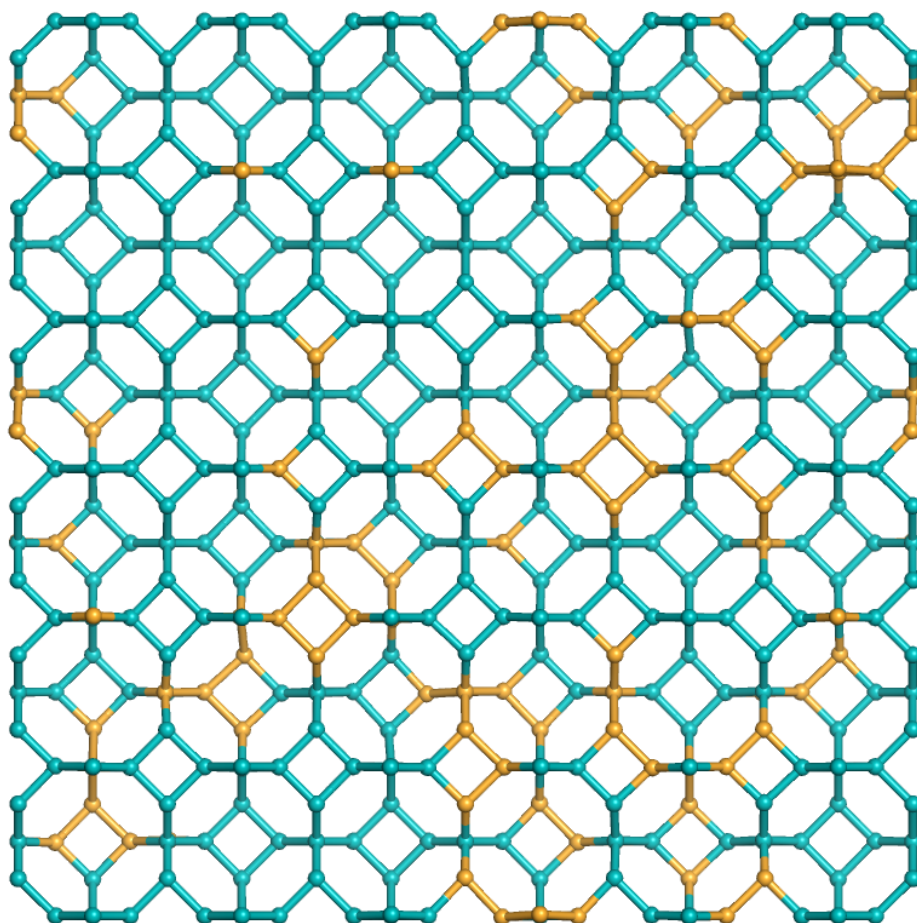


Figure S22: Representative RMC cation distribution for $x = 0.2$

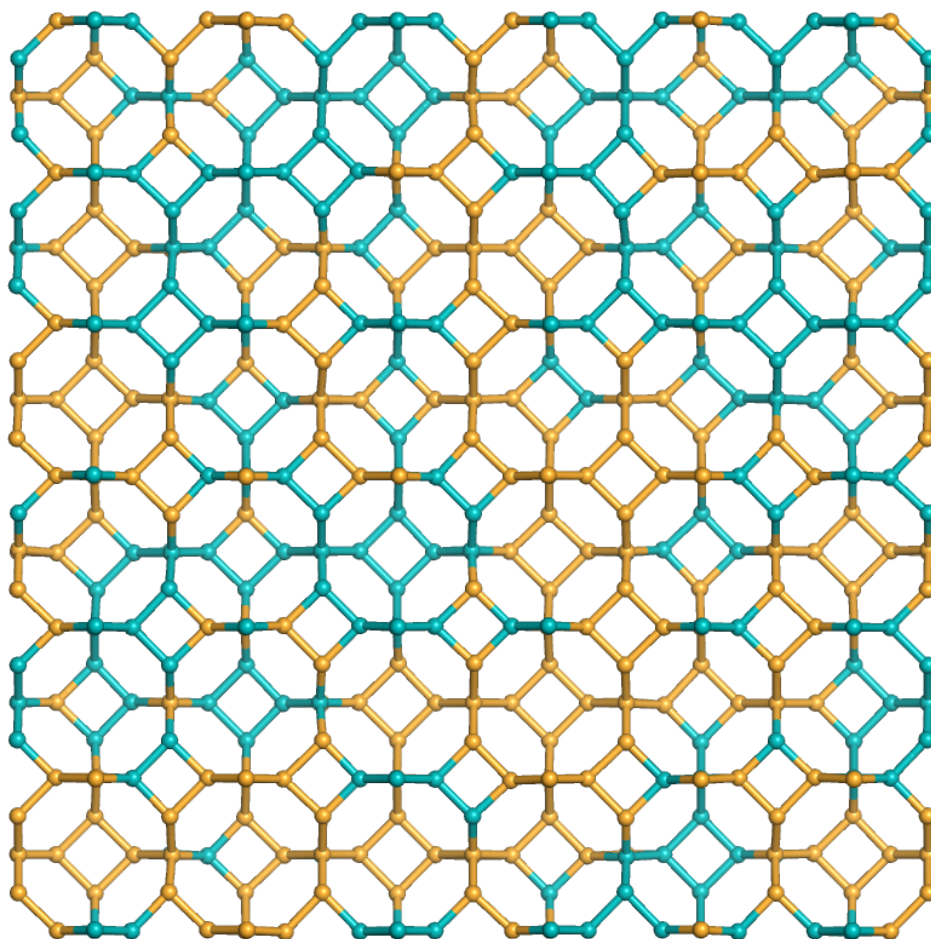


Figure S23: Representative RMC cation distribution for $x = 0.5$

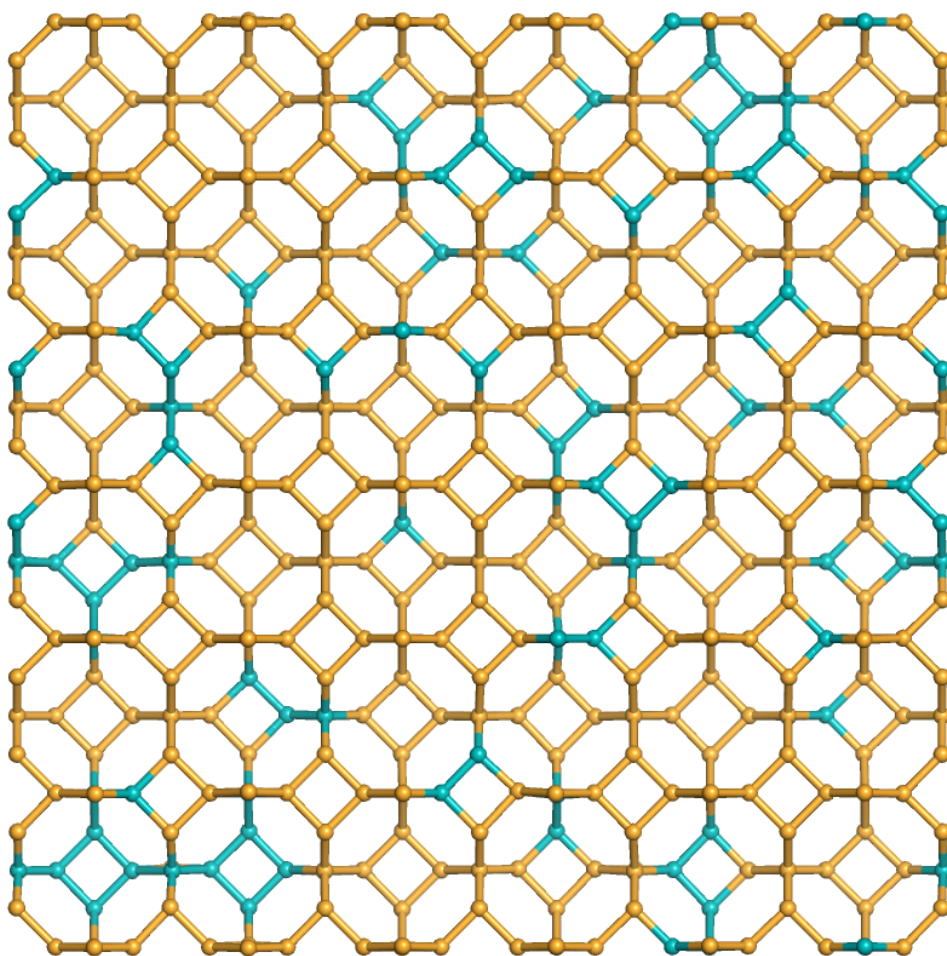


Figure S24: Representative RMC cation distribution for $x = 0.8$

8 References

- (S1) Sun, J. *et al.*, *Microporous and Mesoporous Mater.*, **2018**, *264*, 35–42.
- (S2) Tian, Y.-Q. *et al.*, *Chem. Eur. J.*, **2010**, *16*, 1137–1141.
- (S3) Cliffe, M. J. *et al.*, *J. Appl. Cryst.*, **2012**, *45*, 1321–1329.
- (S4) A. A. Coelho, *TOPAS-Academic, version 4.1 (computer software)*, Coelho Software, Brisbane.
- (S5) Lee, D. D. *et al.*, *Nature*, **1999**, *401*, 788-791.
- (S6) Berry, M. W. *et al.*, *Comp. Stat. Data Anal.* **2007**, *52*, 155-173.
- (S7) Donlan, E. A. *et al.*, *Chem. Commun.* **2017**, *53*, 11233-11236.
- (S8) Metropolis, N. *et al.*, *J. Chem. Phys.* **1953**, *21*, 1087-1092.
- (S9) McGreevy, R. L. and Pusztai, L., *Mol. Simul.* **1988**, *1*, 359-367.